

Geometric localization of thermal fluctuations in red blood cells

Arthur A. Evans^{a,1}, Basanta Bhaduri^{b,c}, Gabriel Popescu^c, and Alex J. Levine^{d,e,f}

^aDepartment of Mathematics, University of Wisconsin–Madison, Madison, WI 53706; ^bDepartment of Applied Physics, Indian School of Mines Dhanbad, Jharkhand 826004, India; ^cQuantitative Light Imaging Laboratory, Beckman Institute for Advanced Science and Technology, University of Illinois at Urbana–Champaign, Urbana, IL 61801; ^dDepartment of Physics and Astronomy, University of California, Los Angeles, CA 90095; ^eDepartment of Chemistry and Biochemistry, University of California, Los Angeles, CA 90095; and ^fDepartment of Biomathematics, University of California, Los Angeles, CA 90095

Edited by David A. Weitz, Harvard University, Cambridge, MA, and approved January 24, 2017 (received for review August 8, 2016)

The thermal fluctuations of membranes and nanoscale shells affect their mechanical characteristics. Whereas these fluctuations are well understood for flat membranes, curved shells show anomalous behavior due to the geometric coupling between in-plane elasticity and out-of-plane bending. Using conventional shallow shell theory in combination with equilibrium statistical physics we theoretically demonstrate that thermalized shells containing regions of negative Gaussian curvature naturally develop anomalously large fluctuations. Moreover, the existence of special curves, “singular lines,” leads to a breakdown of linear membrane theory. As a result, these geometric curves effectively partition the cell into regions whose fluctuations are only weakly coupled. We validate these predictions using high-resolution microscopy of human red blood cells (RBCs) as a case study. Our observations show geometry-dependent localization of thermal fluctuations consistent with our theoretical modeling, demonstrating the efficacy in combining shell theory with equilibrium statistical physics for describing the thermalized morphology of cellular membranes.

red blood cells | shell structures | geometric mechanics | thermal fluctuations | membrane fluctuations

Geometric mechanics, and in particular the century-old theory of thin shells, has seen a resurgence in recent technological applications at length scales spanning several orders of magnitude. Thin elastic surfaces that are curved in their stress-free state display a host of intriguing and useful properties, such as geometry-induced rigidity, bistability, and anisotropic momentum transport (1–5). The general applicability of the mechanics of curved surfaces has wide-ranging consequences for biological functionality as well; it has been used to describe the desiccation of pollen grains, the mechanics of viral capsids, and RBCs (6–9).

The effect of geometry on biological membranes is particularly interesting, because these structures are typically soft enough to support large undulations in thermal equilibrium. Moreover, biology provides a plethora of complex membrane shapes, including the endoplasmic reticulum (10, 11) and the membrane of RBCs. The role of geometry in determining the spatial distribution of their surface undulations is not currently understood, and there may be important implications for biomembrane morphology arising from the use of geometry to control the spatial distribution of thermal undulations.

The case of RBCs is particularly instructive. It provides a unique testing ground for understanding the effect of geometry on thermal undulations of elastic shells because RBCs are both soft enough to have significant thermal undulations and naturally have a complex geometry. The RBC membrane is made up of a lipid bilayer containing transmembrane proteins linked into a 2D triangular network on the cytosolic side of the membrane by spectrin proteins. However, on scales much larger than either the thickness of the membrane or the lattice constant of the spectrin network (12, 13), the composite membrane may be treated as an elastic shell. This shell controls the elasticity of RBCs, because they lack a space-filling internal cytoskeleton.

Based on this simplified elastic description and the assumption of flat membranes, a basic theory for RBC undulatory dynamics was proposed by Brochard and Lennon (12). Subsequent exploration of RBC membrane elasticity has included micropipette aspiration (14), electric field-induced deformation (15), optical tweezers (16), and microrheology, which uses the observed thermal undulations of the membrane to infer elastic moduli (9, 17–20). These last studies, which did not fully account for RBC geometry, found an unexpectedly complex spatial distribution of membrane undulations. Very little was understood about the effects of curvature in altering the mechanical properties and equilibrium fluctuation spectrum of the membrane.

In this paper we develop an elasticity theory of curved surfaces subject to thermal fluctuations and describe how this framework can be applied to geometrically complex objects. Although our theory is developed quite generally for any elastic shell, we consider specifically its application to RBC fluctuations, using data collected from diffraction phase microscopy (DPM) measurements of RBCs. These data produce high-resolution images of RBC flicker maps, which show a spatial distribution of membrane undulations. This distribution is correlated with the curvature of the cells. We demonstrate that this distribution can be quantitatively explained by the theory, without an appeal to active forces or heterogeneous membrane composition.

Our analysis uncovers two generic geometric features that control the mechanics of membranes: the sign of the Gaussian curvature, which qualitatively affects cell deformation, and the existence of singular lines (SLs) where the Gaussian and normal

Significance

Cell shapes are related to their biological function. More generally, membrane morphology plays a role in the segregation and activity of transmembrane proteins. Here we show geometric implications regarding how cellular mechanics plays a role in localizing thermal fluctuations on the membrane. We show theoretically that certain geometric features of curved shells control the spatial distribution of membrane undulations. We experimentally verify this theory using discocyte red blood cells and find that geometry alone is sufficient to account for the observed spatial distribution of fluctuations. Our results, based on statistical physics and membrane elasticity, have general implications for the use of membrane shape to control thermal undulations in a variety of nanostructured materials ranging from cell membranes to graphene sheets.

Author contributions: A.A.E., G.P., and A.J.L. designed research; A.A.E., B.B., G.P., and A.J.L. performed research; A.A.E. analyzed data; and A.A.E. and A.J.L. wrote the paper.

The authors declare no conflict of interest.

This article is a PNAS Direct Submission.

Freely available online through the PNAS open access option.

¹To whom correspondence should be addressed. Email: artio.evans@gmail.com.

This article contains supporting information online at www.pnas.org/lookup/suppl/doi:10.1073/pnas.1613204114/-DCSupplemental.

curvatures simultaneously vanish. The former has been shown to determine localized and extended static deformations and to guide the propagation of undulatory waves on curved surfaces (1, 4). The importance of the latter, particularly in regard to the mechanics of cell membranes, has not been adequately appreciated, although it has been discussed in the context of isometric deformations of axisymmetric shells (21–23) and the folding of creased shells (5). The RBC geometry includes an SL, which leads to the localization of undulations in its vicinity and dominates the structure of the RBC flicker maps. Neither flat membranes, where stretching and bending deformation modes decouple, nor shells of strictly positive Gaussian curvature admit these geometrically induced, anomalously soft regions.

Thermalized Shallow Shell Theory

We begin by examining the response of an elastic shell subjected to normal forces. The resulting Green's function provides insight into the spectrum of undulatory modes of the surface. We will later address the spatial distribution of thermal fluctuations on RBCs using this understanding of the equilibrium population of undulatory fluctuations. In general, the elastic theory of shells (materials that are curved in their unstressed state) is remarkably complex (24, 25). Solving the full problem is formidable, if not impossible; for our purposes we consider small-amplitude undulations on a surface that is only gently curved (i.e., the local radius of curvature is much greater than the wavelength of deformation). In this case, the full nonlinear problem of elastostatics is known to reduce to the linearized Donnell–Mushtari–Vlasov (DMV) equations for a “shallow shell” (25) (see [Supporting Information](#) for a detailed derivation):

$$B\nabla^4\zeta - \mathcal{L}[\chi] = f(\mathbf{r}), \quad [1]$$

$$\frac{1}{S}\nabla^4\chi + \mathcal{L}[\zeta] = 0. \quad [2]$$

Here ∇^2 is the Laplacian operator, ∇^4 is the biLaplacian, and $\zeta(\mathbf{r})$ defines the normal deflection of the shell from its reference state, given by the 3D vector \mathbf{r} . The in-plane stress is given in terms of an Airy stress function χ , and the two elastic constants B and S represent the bending and stretching moduli of the shell, respectively, and f is the applied normal load.

Eq. 1 ensures normal stress balance across the shell. In-plane stress is identically satisfied due to the function χ , and the linear differential operator $\mathcal{L} = \epsilon^{\alpha\eta}\epsilon^{\beta\xi}d_{\alpha\beta}\partial_\eta\partial_\xi$ contains all of the curvature information from the surface, where $d_{\alpha\beta}$ is the curvature tensor of the undeformed shape, and $\epsilon^{\alpha\beta}$ is the antisymmetric tensor. We must also include a compatibility condition via Eq. 2, which ensures the surface is physically realizable. In the limit of a flat membrane where \mathcal{L} vanishes, this condition reduces to the biharmonic equation, which the Airy stress function must satisfy for stress balance (26).

The operator \mathcal{L} is the primary source for coupling between curvature and elasticity, because it mixes in-plane stress and out-of-plane deformation through the curvature of the surface. It takes the form

$$\mathcal{L} = \left(\frac{1}{R_y}\partial_x^2 + \frac{1}{R_x}\partial_y^2 \right) \quad [3]$$

in a local Cartesian coordinate system $\{x, y\}$ aligned with the principal curvature directions on the undeformed membrane with corresponding radii of curvature $R_{x,y}$. We observe from Eq. 3 that the coupling of normal to in-plane stress vanishes in the limit of a flat reference state $\mathcal{L} \rightarrow 0$ when $R_{x,y} \rightarrow \infty$; there is no in-plane stretching of a flat membrane in response to normal loading. The curvature of the stress-free membrane, however, couples stretching and bending, and thus curvature influences the mechanics of normal deformation. The primary cause of

this behavior arises from the Gaussian curvature $K = 1/(R_x R_y)$. When K changes sign, the operator \mathcal{L} changes type, which leads to vastly different mechanical deformation characteristics (1, 4).

The mechanics of the shell are controlled by two elastic constants. For thin shells treated as elastic continua, these are related to the Young's modulus Y , Poisson's ratio ν , and thickness t . One finds that $B \sim Yt^3$ and $S \sim Yt$, showing that sufficiently thin sheets are more compliant to bending than to stretching. The relative importance of bending to stretching energies on a membrane with local radius of curvature R can be quantified by the dimensionless Föppl–von Kármán number $\gamma \equiv SR^2/B \sim (R/t)^2$. Many materials, such as graphene sheets (27), viral capsids (7, 28, 29), and the tethered lipid bilayer of RBCs lack a well-defined 3D material analog; nevertheless, the 2D elastic constants remain well-defined. Effective elastic constants of RBCs have been measured in a variety of ways (14, 20, 30) yielding $B \sim 5.5k_B T$ and $\hat{\mu} \sim 7.5\mu\text{N/m}$, which results in $\gamma \sim 10^3$.

Consider first the case of uniform membrane uniform curvature. It is convenient to work in the Fourier domain, such that $\zeta(\mathbf{r}, t) = \int \hat{\zeta}(\mathbf{q}, \omega) e^{i(\mathbf{q}\cdot\mathbf{r} - \omega t)} d^2\mathbf{q}d\omega$. To consider the fluctuations of the membrane in the overdamped limit (appropriate to the case of RBCs) we write the normal load in Eq. 1

$$f(\mathbf{r}) = -\xi(\mathbf{r})\partial_t\zeta + \eta(\mathbf{r}, t), \quad [4]$$

where $\xi(r)$ is the hydrodynamic resistance function and η is the Brownian force. Computing the resistance function for an arbitrarily curved membrane is challenging, but unnecessary, if we restrict our analysis to equilibrium fluctuations [this is a result of the fluctuation-dissipation theorem (31)]. This more general Langevin description facilitates future work on time-dependent height correlations in equilibrium (20) and all correlations in nonequilibrium (e.g., pump-driven membranes) (32). In a viscous medium we may write the second moment of the force fluctuations in thermal equilibrium as $\langle \eta(\mathbf{r}, t)\eta(\mathbf{r}', t') \rangle = 2D(\mathbf{r} - \mathbf{r}')\delta(t - t')$, where the magnitude $D(\mathbf{r})$ is such that in the Fourier domain $D(\mathbf{q})\xi(\mathbf{q}) = k_B T$. Here and throughout we use the angled brackets to denote averages over an ensemble of equilibrium states at temperature T ; k_B is Boltzmann's constant.

Using Eqs. 1 and 2 to eliminate the stress function in favor of the normal displacement and making use of Eq. 4 we write a Langevin equation for the membrane undulations in terms of the response function $G(\mathbf{q}, \omega)$ as

$$\zeta(\mathbf{q}, \omega) = G(\mathbf{q}, \omega)\eta(\mathbf{q}, \omega), \quad [5]$$

where

$$G(\mathbf{q}, \omega) = \frac{1}{Bq^4 + Sm^2(\hat{q}) - i\omega\xi(\mathbf{q})}, \quad [6]$$

and the Gaussian noise has zero mean and a second moment given by $\langle \eta(\mathbf{q}, \omega)\eta(\mathbf{q}', \omega') \rangle = 2D(\mathbf{q})\delta(\mathbf{q} + \mathbf{q}', \omega + \omega')$.

We see from the response function that the spectrum of undulatory modes is gapped by $m(\hat{q}) = R_x^{-1}(\beta \cos^2 \theta_q + \sin^2 \theta_q)$, where $\beta = R_x/R_y$ measures the curvature anisotropy of the membrane. The unit vector $\hat{q} = \mathbf{q}/|\mathbf{q}| = (\cos \theta_q, \sin \theta_q)$ defines an angle θ_q between the wavevector and the direction of principal curvature R_x . For membranes with positive Gaussian curvature $\beta > 0$, the gap in the spectrum remains finite for all wavevectors. For negative Gaussian curvature, however, $\beta < 0$ and the gap vanishes along the special directions $\theta_q^* = \pm \arctan(\sqrt{-\beta})$. In the language of differential geometry, these “asymptotic directions” correspond to curves with zero normal curvature. Implications for the mechanics of these curves include extended deformations, preferential flexural wave propagation, and folding without stretching (1, 4, 5). We will return to this point in our discussion of the undulations of the RBC.

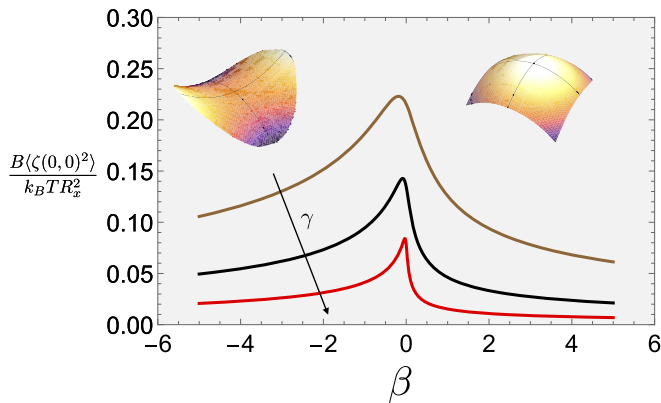


Fig. 1. Equilibrium variance of normal displacement as a function of the curvature anisotropy $\beta = R_x/R_y$. Insets show the schematic shape of the surface for positive and negative β . The integral in Eq. 7 is evaluated using a low-wavenumber cutoff of $q = \pi$ and a high-wavenumber cutoff of $q = \pi\sqrt{\gamma}$, in dimensionless units. The Föppl-von Kármán number increases in the direction indicated by the arrow, corresponding to values of $\gamma = 10^3, 10^4, 10^5$. For increasing γ , the increased importance of stretching over bending leads to an overall decay in the magnitude of the fluctuations, but the peak at $\beta = 0$ sharpens.

We now compute the equilibrium height fluctuations by integrating over all frequencies and wavenumbers. To do so we introduce a short distance cutoff set by the thickness of the membrane t and a long distance cutoff set by the lateral extent of the membrane L , which in the shallow theory that we consider is

appropriately given by $L \sim R_x$: $\pi/R_x < |\mathbf{q}| < \pi/t$. Nondimensionalizing the wavevector $q \rightarrow qR_x$ so that the available range of wavenumbers is given by $\pi < q < \pi\sqrt{\gamma}$, the variance of the equilibrium height fluctuations is given in terms of the dimensionless integral $\mathcal{I}(\gamma, \beta)$ (see *Supporting Information* for details):

$$\langle |\zeta(0,0)|^2 \rangle = \frac{k_B T R_x^2}{B} \mathcal{I}(\gamma, \beta), \quad [7]$$

$$\mathcal{I}(\gamma, \beta) = \int_{\pi}^{\pi\sqrt{\gamma}} \int_0^{2\pi} \frac{q dq d\theta}{q^4 + \gamma(\beta \cos^2 \theta + \sin^2 \theta)^2}. \quad [8]$$

Note that as $S \rightarrow 0$ the fluctuation spectrum reduces to the Brochard-Lennon result for erythrocyte flicker (12), and for $S > 0$ with $\beta = 1$ we recover the bare response function of an unpressurized spherical shell (33).

Asymptotically we may evaluate how the magnitude of fluctuations scale with both the curvature anisotropy β and the Föppl-von Kármán number γ (see *Supporting Information* for details). In the limit of large system size, $\mathcal{I}(\gamma, 0)$ diverges as $q \rightarrow 0$, which is to be expected because such a shell is cylindrical and thus has a single special direction (along the axis of symmetry) where it responds to undulations like a flat plate; for a free plate, the fluctuation spectrum diverges as q^{-4} (12). When $\beta > 0$, the stretching term dominates for low wavenumber, and the lower limit on the wavenumber may be replaced as $q \rightarrow 0$, yielding $\mathcal{I}(\gamma, \beta) \sim \beta^{-1/2} \gamma^{-1/2}$. For $\beta < 0$, the integral is weakly divergent as $q \rightarrow 0$, resulting in $\mathcal{I}(\gamma, \beta) \sim \beta^{-1/2} \gamma^{-1/2} \ln(L/t)$. With $L \sim R$ this implies $\mathcal{I}(\gamma, \beta) \sim \beta^{-1/2} \gamma^{-1/2} \ln \gamma$. This difference in scaling behavior arises from the nongapped, extended

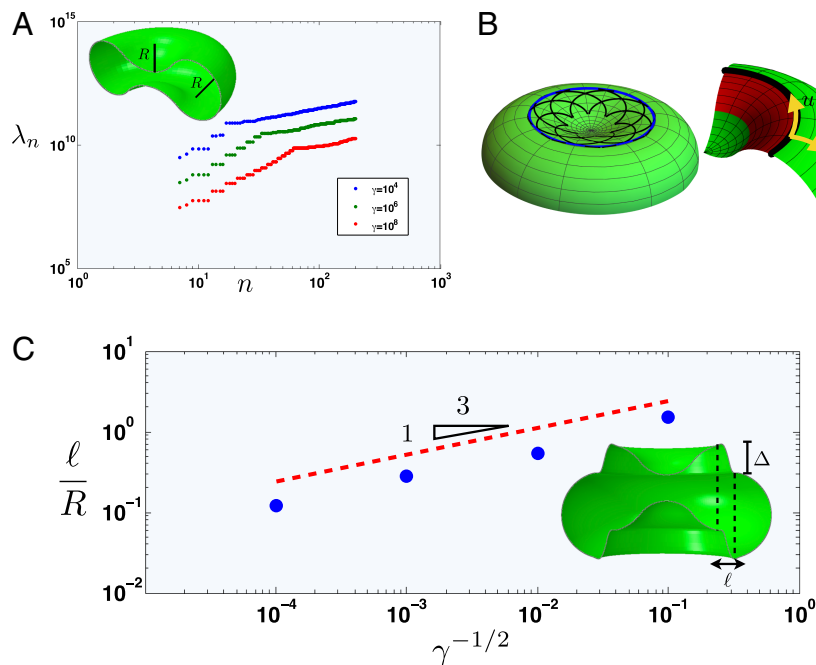


Fig. 2. Mode spectrum. (A) The eigenvalue spectrum for a freestanding shell as a function of mode number n , for various γ . (Inset) Axisymmetric shell generated from circular arcs of radius R revolved around a central axis. (B) (Left) The asymptotic curves of a biconcave shell exist only within regions that have negative Gaussian curvature (black lines). Asymptotic curves terminate at the inner boundary as the Gaussian curvature goes to zero. At the outer boundary, however, the asymptotic curves are locally tangent to the boundary between negative and positive Gaussian curvature. This indicates the presence of an SL, where in-plane stress cannot propagate without regularizing bending energy effects. (Right) Schematic of the local coordinate system for evaluating the boundary layer scaling near SLs. The green regions of the shell have positive Gaussian curvature, and the red is the band of negative Gaussian curvature. (C) A boundary layer develops across SLs to regularize stress propagation. The size of this layer scales with γ , as shown numerically. (Inset) Fundamental mode of a free-standing elastic erythrocyte is almost rigid body motion of two surfaces partitioned by the SL. The amplitude of the deformation is arbitrary in a linear mode analysis and has been enlarged to be visible in the figure. Given the boundary layer size ℓ and a vertical displacement Δ , the effective stiffness of such a deformation can be estimated (discussed in the text).

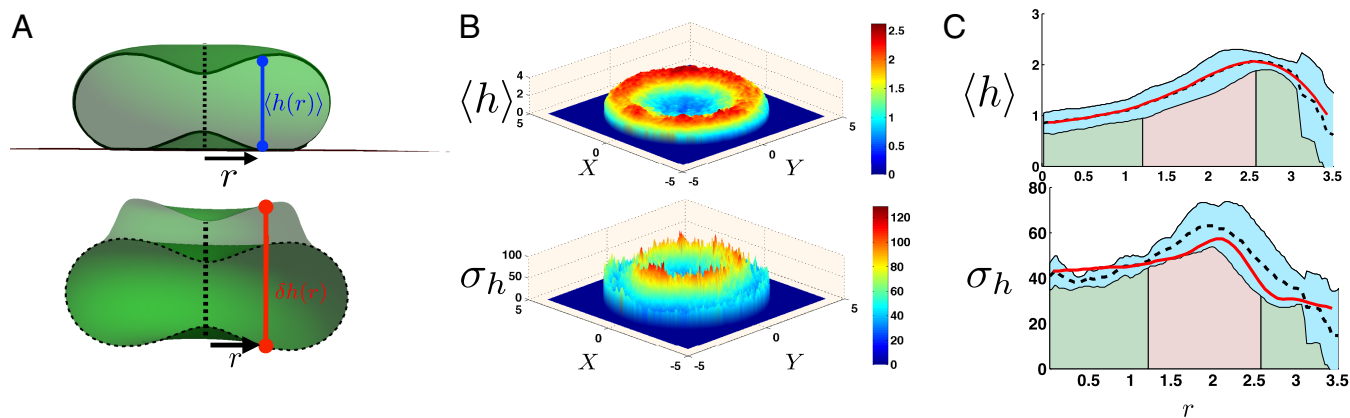


Fig. 3. Thermalized RBCs examined using DPM. (A) (Top) Schematic of human erythrocyte adhered to a glass substrate. The thickness $h(r)$ of the cell is measured instantaneously as a function of position using DPM. (Bottom) A schematic of how DPM measures fluctuations in soft cells. Deviations from the average height $\langle h(r) \rangle$ are measured as $\delta h(r)$, and the difference in optical path length is converted directly into a change in height. Note that the change in cell thickness is not equivalent to the normal displacement of the cell $\zeta(r)$, which deviates from the substrate normal when the cell is substantially curved. (B) (Top) Average thickness for a representative cell, displaying the characteristic biconcave shape of healthy RBCs. (Bottom) Average fluctuations for a representative cell. The SD of the cell heights used to determine the fluctuations. The fluctuation profile depends on the radial distance r from the center of the cell. (C) Radial and ensemble-averaged height profiles for RBCs (dashed line) and associated SD (blue region). Theoretical curves from our finite element model described below are shown as red lines.

deformations that occur in saddle-shaped shells. These extended deformations have direct consequences for the spectrum of complete shells, addressed in more detail next. In Fig. 1 we compute numerically the value of the integral in Eq. 7 and find equilibrium height fluctuations as a function of β for various values of the Föppl-von Kármán number. For $\beta \neq 0$ the fluctuations scale as predicted, whereas the fluctuations are enhanced near the $\beta \approx 0$ region. Physically, we expect that shells containing different signs of Gaussian curvature (so-called shells of mixed type) to exhibit qualitatively dissimilar regions of fluctuations.

The Elastic Erythrocyte Model

We have so far examined the effect of spatially uniform surface geometry on undulations. This simplification is reasonable in cases where the wavelength of the undulations is very small compared with both the smallest radius of curvature and the scale over which that curvature is changing. In the presence of boundary conditions or spatially heterogeneous curvature, as is certainly the case in RBCs, a more complete shell formulation is required.

We begin numerically by creating a finite element model for a linearly elastic shell of mixed type. For simplicity, we use an axisymmetric shell that is generated from a planar curve. This curve is composed of two circular arcs of the same radius R , so that there is no ambiguity in defining a Föppl-von Kármán number. It can be written as a piecewise function in terms of an arc length variable s , with a curve $\mathbf{C}(s) = R \{r(s), z(s)\}$:

$$\mathbf{C}(s) = \begin{cases} \{\sin s, 2 \cos s_1 - \cos s\}, & s \leq s_1 \\ \{\sin s + 2 \sin s_1, -\cos s\}, & s_1 + \pi \leq s \leq \pi/2. \end{cases} \quad [9]$$

We scale the size of the curve by the radius of curvature R and choose the single parameter s_1 to match approximate RBC sizes. Fig. 2A, Inset shows the axisymmetric shell generated by revolving the curve about the z axis for $R = 1.4 \mu\text{m}$ and $s_1 = \pi/4$. Although this shell has nonconstant Gaussian curvature, the mechanics may be characterized in terms of a single dimensionless Föppl-von Kármán number: $\gamma = SR^2/B$.

Using this 3D model we perform a mode analysis in ABAQUS (Dassault Systèmes), calculating the eigenvalues and eigenmodes associated with free vibration. For a free-standing membrane, we find that there are two distinct classes of eigenvalues (Fig. 2A).

This distinction becomes sharper at high γ (34), where the softest modes involve large portions of the RBC undergoing essentially rigid body motions, and coupled only through a thin boundary layer (Fig. 2C, Inset). In these lowest-frequency modes, deformation is localized near boundaries between negative and positive Gaussian curvature. Based on our above analysis, we expect to see such large deformation in regions where the Gaussian curvature approaches zero, as is necessarily found near the boundaries on the membrane where the Gaussian curvature changes sign.

However, there are two such boundaries in the elastic erythrocyte model, and the localization of large-amplitude bending occurs near only one of them. To understand this, one must consider the asymptotic curves of a surface and a special subset of such curves that we call SLs (21–23). Asymptotic curves on the surface are those along which the osculating plane of the curve is locally tangent to the surface (Fig. 2B, Left), where the asymptotic curves are shown as black lines. These directions correspond to the special directions θ_q^* derived earlier for surfaces with spatially constant curvature. When an asymptotic curve has zero Gaussian curvature as well (e.g., the blue line in Fig. 2B, Left) it is an SL [although they have been referred to as “crowns” or “rigidifying curves” in other contexts (21–23)]. Along such lines, the shell equations become geometrically singular in that the undulations there are enhanced just as they are on a flat $\beta = 0$ membrane in the uniform curvature theory. The low-frequency or “soft” modes of a geometrically complex membrane are dominated by large length scale nearly rigid body motions of regions of the membrane separated by these SLs, which serve as a locus for weak, bending-dominated couplings between the stiffer regions. As a consequence, the spatial distribution of SLs controls the low-frequency undulatory spectrum of geometrically complex membranes.

To further examine the peculiar behavior of undulations near SLs we consider the two curves on an elastic RBC where the Gaussian curvature of the shell changes sign (Fig. 2B). Defining a local coordinate system $\{u, v\}$ along these curves, we use the DMV equations to characterize the singular nature of the shell equations about these curves. The inner curve is not singular, even though it is a boundary between different signs of Gaussian curvature. The outer curve, however, requires further analysis. Near the outer curves the shell appears toroidal, with

$1/R_u \approx v/R^2$, $1/R_v \approx 1/R$. If we consider only the most singular terms, the DMV equations become

$$B\partial_v^4\zeta - \frac{v}{R^2}\partial_v^2\chi = \eta, \quad \frac{1}{S}\partial_v^4\chi + \frac{v}{R^2}\partial_v^2\zeta = 0. \quad [10]$$

We rescale variables $\bar{\zeta} = \zeta/R$, $\bar{\chi} = \chi/B$, and $\bar{v} = v/\ell$, where ℓ is the characteristic size of the boundary layer. Eliminating $\bar{\chi}$ and keeping only the most singular terms yields the dominant balance of $\gamma\ell^6 \sim R^6$. For an elastic membrane with well-defined thickness this gives $\ell \sim t^{1/3}R^{2/3}$, as calculated for toroidal shells elsewhere (22). Our finite element analysis is consistent with this scaling as shown in Fig. 2C. We may also calculate the energy content of this boundary layer. Because bending energy regularizes the divergence in the stress, the bending energy dominates the contribution in the layer. Bending energy in a curved shell with vertical displacement Δ (Fig. 2C, *Inset*) is given by $E_B \sim \int B(1/R_u + 1/R_v)^2 dA \sim B(\Delta/\ell^2)^2(R\ell) \sim (BR/\ell^3)\Delta^2$. This indicates an effective stiffness $k_{eff} \sim S\gamma^{-1/2}$ in general, or $k_{eff} \sim Yt^2/R$ for a shell with well-defined thickness. As noted by Audoly and Pomeau (22), this mode of deformation, arising from geometric conditions in shells, has an anomalous stiffness in between stretching ($k_{eff} \sim S$) and bending ($k_{eff} \sim S/\gamma$).

DPM

Finally, we compare our geometric model to measurements performed using DPM, which allows for high temporal and spatial resolution of the RBC thermal fluctuations (35, 36) (see [Supporting Information](#) for details and Fig. S1 for experimental schematic). DPM measures the phase change accumulated through fluctuating surfaces. Because the index of refraction of the RBC interior is spatially homogeneous, changes in the optical path length $\delta h(r)$ (Fig. 3A) correspond directly to changes in the cell's thickness projected along the path of the light. Thus, DPM can observe membrane fluctuations on the order of 10 nm, but is insensitive to surface deformations that do not change the path length through the cell (e.g., a mode generating a symmetric displacement of the membrane at diametrically opposed points on the cell boundary). The fundamental mode of deformation for the free-standing elastic RBC in the previous section (Fig. 2C, *Inset*) is thus invisible to DPM because of the pseudorigid body deformation. Attaching the cell to a substrate introduces pinned boundary conditions and the points of contact changing the fundamental deformation mode [compare the sketches at the bottom of Fig. 3A (pinned at the substrate) to that in Fig. 2A, *Inset* (no substrate)].

Typical datasets for both the average height profile $\langle h \rangle$ and the SD $\sigma_h = \sqrt{\langle (h - \langle h \rangle)^2 \rangle}$ are shown in Fig. 3B. The height data reproduce the characteristic biconcave shape of most healthy RBCs, whereas the fluctuations are localized in a band at finite radius from the axis of symmetry. We collected data from a small ensemble of five cells and obtained averages (over all cells and over azimuthal directions about the cells' symmetry axis) and SDs for $\langle h \rangle$, σ_h (see Fig. 3C, *Top*, where the dashed black lines represent the average height and the blue bands represent sample SDs). In Fig. 3C, *Bottom* we show the SD of the fluctuations about these mean heights $\sqrt{\langle h^2(r) \rangle}$. The green and red regions denote calculated regions of positive and negative Gaussian curvature, respectively. The fluctuations clearly peak in the region of negative Gaussian curvature, as expected.

To quantitatively compare with our model predictions we construct a more specific finite element model using the precise geometric data of the RBC. Taking the ensemble-averaged height field from the experimental data in Fig. 3C we generate a smoothed, axisymmetric shell model. We first extract the height field corresponding to the dashed black line and truncate the model at $r = 3\mu\text{m}$, because substantial lateral fluctua-

tions lead to enhanced experimental error for larger radii. By reflecting this height profile vertically and connecting the exterior portions of the curve with a circular arc we generate a complete axisymmetric shell from the RBC shape data. Using existing values for the elastic moduli of RBCs (20) we perform another eigenvalue analysis, as in the previous section. With pinned boundary conditions on the lowest point of the shell representing adhesive contact with the substrate, we generate eigenvalues and eigenmodes $\{\lambda_n, \Phi_n\}$, which have a character similar to those of the free-standing elastic erythrocyte. Armed with this eigenvalue spectrum we invoke the equipartition theorem to calculate the fluctuations that would be observed in thermal equilibrium. We write the equilibrium deformation field $\mathbf{u} = \sum_n a_n \Phi_n$, where the amplitudes a_n must satisfy a relationship given by thermodynamic equilibrium. The equipartition theorem guarantees that each of the modes calculated will contain an energy of $k_B T/2$, and thus the amplitudes a_n must satisfy $\langle a_n a_m \rangle = \frac{1}{2}(k_B T/\lambda_n)\delta_{nm}$. Nondimensionalizing the eigenvalues so that $\lambda_n = (B/\ell^2)\Lambda_n$, with ℓ the boundary layer thickness, yields the height profile variance

$$\sigma_h^2 = \frac{k_B T \ell^2}{B} \sum_n \frac{|\Phi_n \cdot \hat{\mathbf{z}}|^2}{\Lambda_n}, \quad [11]$$

where we have taken the appropriate projection with the unit vector $\hat{\mathbf{z}}$ to project deformations onto the changing optical path length. The red line in Fig. 3C, *Bottom* corresponds to these predicted fluctuations. We find that they are consistent with those observed by DPM with no free fitting parameters. We conclude that one can understand the spatial distribution of thermal undulations on the RBC with a minimal model that assumes all spatial variation results from geometry alone; the elastic properties of the cell membrane may be assumed to be spatially homogeneous.

Summary

The geometry of the undeformed reference state of an elastic shell strongly affects the spectrum of its undulatory modes. In particular, the existence of SLs on surfaces with spatially inhomogeneous curvature, ones that include boundaries between regions of positive and negative Gaussian curvature, introduces a set of low-frequency modes of the surface. One can understand the appearance of these low-frequency states from an analysis of linearized shallow shell theory, as expressed in the DMV equations of the surface.

Because the spectrum of soft modes dominates the fluctuations and linear response of many-body systems, the existence and distribution of sets of SLs on membranes of complex geometry is the principal feature through which geometry controls the statistical physics of such structures.

There is an ongoing discussion regarding whether RBC fluctuations are strongly affected by nonequilibrium processes, specifically ATP-consuming pumps (12, 13, 17, 20, 32, 33, 37–40). This question is difficult to address experimentally because it is clear that ATP depletion has a number of effects on the RBC membrane, including large-scale geometric transitions such as the formation of spherocytes. The agreement of our experiments with an analysis of the predicted fluctuation spectrum in thermal equilibrium suggests that the large-scale deformation modes, which form the dominant contribution to the observed local height fluctuations, can be accounted for without recourse to nonequilibrium noise. This does not imply that nonequilibrium processes are irrelevant but suggests that they might couple strongly only to the short-wavelength modes, to which our experiments are less sensitive. Studying these nonequilibrium dynamics will be challenging, because one is then required to account for hydrodynamic dissipation in the cytosol and the fluid surrounding the cell. Such hydrodynamic interactions have been studied only for

the simpler cases of flat (12) and spherical membranes (8, 33). In addition, dissipation within the membrane (membrane viscoelasticity) would have to be addressed.

The most direct implication of this work is that membrane microrheology experiments must take into account the global geometry of the membrane. Because local geometry controls fluctuations, one may also imagine that there is selective pressure on cell membrane morphology to control the spatial distribution of its thermal (and nonthermal) motion. For example, intercellular junctions (e.g., synapses) may be engineered to suppress fluctuations and thereby minimize the disjoining pressure at these junctions.

Our results have direct implications on engineering membrane geometry to localize or guide thermal undulations in both biological and synthetic systems. One synthetic system, graphene sheets, is of particular interest. Here one finds a direct cou-

pling between geometry and their electronic properties (41, 42). We anticipate that one may be able to modify the coupled fluctuations of the surface and local electrochemical potential through curvature in graphene. Finally, we observe that the coupling of curvature to mechanics in the presence of thermal fluctuations suggests that renormalization of area and bending moduli due to nonlinear terms in equations of motion may be affected by nontrivial curvature of the elastic reference state of the membrane, and thus provide a way in which complex membrane geometry at long length scales serves to create spatial variations in the effective elastic moduli of the thermalized membrane.

ACKNOWLEDGMENTS. This work was supported by National Science Foundation (NSF) Grants CBET-0939511 STC, DBI 14-50962 EAGER, IIP-1353368 (to G.P.), DMR-1309188 (to A.J.L.), and DMR-1121288 (MRSEC) (to A.A.E.).

- Vaziri A, Mahadevan L (2008) Localized and extended deformations of elastic shells. *Proc Natl Acad Sci USA* 105(23):7913–7918.
- Lazarus A, Florijn HCB, Reis PM (2012) Geometry-induced rigidity in nonspherical pressurized elastic shells. *Phys Rev Lett* 109(14):144301.
- Vella D, Ajdari A, Vaziri A, Boudaoud A (2012) Indentation of ellipsoidal and cylindrical elastic shells. *Phys Rev Lett* 109(14):144302.
- Evans AA, Levine AJ (2013) Reflection and refraction of flexural waves at geometric boundaries. *Phys Rev Lett* 111:038101.
- Bende NP, et al. (2015) Geometrically controlled snapping transitions in shells with curved creases. *Proc Natl Acad Sci USA* 112(36):11175–11180.
- Katifori E, Alben S, Cerda E, Nelson DR, Dumais J (2010) Foldable structures and the natural design of pollen grains. *Proc Natl Acad Sci USA* 107(17):7635–7639.
- Lidmar J, Mirny L, Nelson DR (2003) Virus shapes and buckling transitions in spherical shells. *Phys Rev E Stat Nonlin Soft Matter Phys* 68(5):051910.
- Kuriabova T, Levine A (2008) Nanorheology of viscoelastic shells: Applications to viral capsids. *Phys Rev E Stat Nonlin Soft Matter Phys* 77:031921.
- Park Y, et al. (2011) Measurement of the nonlinear elasticity of red blood cell membranes. *Phys Rev E Stat Nonlin Soft Matter Phys* 83(5):051925.
- Terasaki M, et al. (2013) Stacked endoplasmic reticulum sheets are connected by helical membrane motifs. *Cell* 154(2):285–296.
- Güven J, Huber G, Valencia DM (2014) Terasaki spiral ramps in the rough endoplasmic reticulum. *Phys Rev Lett* 113(18):188101.
- Brochard F, Lennon JF (1975) Frequency spectrum of the flicker phenomenon in erythrocytes. *J Phys* 36(11):1035–1047.
- Fournier J-B, Lacoste D, Raphaël E (2004) Fluctuation spectrum of fluid membranes coupled to an elastic meshwork: Jump of the effective surface tension at the mesh size. *Phys Rev Lett* 92(1):018102.
- Discher DE, Mohandas N, Evans EA (1994) Molecular maps of red cell deformation: Hidden elasticity and in situ connectivity. *Science* 266(5187):1032–1035.
- Engelhardt H, Gaub H, Sackmann E (1984) Viscoelastic properties of erythrocyte membranes in high-frequency electric fields. *Nature* 307:378–380.
- Dao M, Lim CT, Suresh S (2003) Mechanics of the human red blood cell deformed by optical tweezers. *J Mech Phys Solids* 51(11):2259–2280.
- Kaizuka Y, Groves JT (2006) Hydrodynamic damping of membrane thermal fluctuations near surfaces imaged by fluorescence interference microscopy. *Phys Rev Lett* 96(11):118101.
- Popescu G, et al. (2005) Erythrocyte structure and dynamics quantified by hilbert phase microscopy. *J Biomed Opt* 10(6):060503.
- Popescu G, et al. (2006) Optical measurement of cell membrane tension. *Phys Rev Lett* 97(21):218101.
- Park Y, et al. (2010) Measurement of red blood cell mechanics during morphological changes. *Proc Natl Acad Sci USA* 107(15):6731–6736.
- Audoly B (1999) Courbes rigidifiant les surfaces. *C R Acad Sci Math* 328(4):313–316.
- Audoly B, Pomeau Y (2002) The elastic torus: Anomalous stiffness of shells with mixed type. *C R Mec* 330(6):425–432.
- Audoly B, Pomeau Y (2010) *Elasticity and Geometry: From Hair Curls to the Nonlinear Response of Shells* (Oxford Univ Press, Oxford).
- Nelson D, Piran T, Weinberg S (2004) *Statistical Mechanics of Membranes and Surfaces* (World Scientific, Singapore).
- Niordson FI (1985) *Shell Theory*. North Holland Series in Applied Mathematics and Mechanics (North-Holland, Amsterdam), Vol 29, p 1.
- Landau LD, Lifschitz EM, Pitaevskii LP, Kosevich AM (1986) *Theory of Elasticity*. Course of Theoretical Physics (Pergamon, Oxford), Vol 7.
- Amorim B, et al. (2015) Novel effects of strains in graphene and other two dimensional materials. *Phys Rep* 617:1–54.
- Gibbons MM, Klug WS (2007) Nonlinear finite-element analysis of nanoindentation of viral capsids. *Phys Rev E Stat Nonlin Soft Matter Phys* 75(3):031901.
- Roos WH, Bruinsma R, Wuite GJL (2010) Physical virology. *Nat Phys* 6(10):733–743.
- Mohandas N, Evans E (1994) Mechanical properties of the red cell membrane in relation to molecular structure and genetic defects. *Annu Rev Biophys Biomol Struct* 23(1):787–818.
- Chaikin PM, Lubensky TC (2000) *Principles of Condensed Matter Physics* (Cambridge Univ Press, Cambridge, UK), Vol 1.
- Betz T, Lenz M, Joanny J-F, Sykes C (2009) ATP-dependent mechanics of red blood cells. *Proc Natl Acad Sci USA* 106(36):15320–15325.
- Paulose J, Vliegenthart GA, Gompfer G, Nelson DR (2012) Fluctuating shells under pressure. *Proc Natl Acad Sci USA* 109(48):19551–19556.
- Peterson MA (1992) Linear response of the human erythrocyte to mechanical stress. *Phys Rev A* 45(6):4116–4131.
- Popescu G, Ikeda T, Dasari RR, Feld MS (2006) Diffraction phase microscopy for quantifying cell structure and dynamics. *Opt Lett* 31(6):775–777.
- Bhaduri B, et al. (2014) Diffraction phase microscopy: Principles and applications in materials and life sciences. *Adv Opt Photonics* 6(1):57–119.
- Tuvia S, et al. (1997) Cell membrane fluctuations are regulated by medium macroviscosity: Evidence for a metabolic driving force. *Proc Natl Acad Sci USA* 94(10):5045–5049.
- Loubet B, Seifert U, Lomholt MA (2012) Effective tension and fluctuations in active membranes. *Phys Rev E Stat Nonlin Soft Matter Phys* 85(3):031913.
- Boss D, et al. (2012) Spatially-resolved eigenmode decomposition of red blood cells membrane fluctuations questions the role of ATP in flickering. *PLoS One* 7(8):e40667.
- Turlier H, et al. (2016) Equilibrium physics breakdown reveals the active nature of red blood cell flickering. *Nat Phys* 12:513–519.
- Kim E-A, Castro Neto AH (2008) Graphene as an electronic membrane. *Europhys Lett* 84(5):57007.
- Kotov VN, Uchoa B, Pereira VM, Guinea F, Castro Neto AH (2012) Electron-electron interactions in graphene: Current status and perspectives. *Rev Mod Phys* 84(3):1067–1125.
- Bhaduri B, Kandel M, Brugnara C, Tangella K, Popescu G (2014) Optical assay of erythrocyte function in banked blood. *Sci Rep* 4:6211.
- Ikeda T, Popescu G, Dasari RR, Feld MS (2005) Hilbert phase microscopy for investigating fast dynamics in transparent systems. *Opt Lett* 30(10):1165–1167.
- Thevenaz P, Ruttimann UE, Unser M (1998) A pyramid approach to subpixel registration based on intensity. *IEEE Trans Image Process* 7(1):27–41.
- Powers TR (2010) Dynamics of filaments and membranes in a viscous fluid. *Rev Mod Phys* 82(2):1607–1631.
- Evans AA, Levine AJ (2015) Membrane rheology. *Complex Fluids in Biological Systems* (Springer, New York), pp 159–186.
- Levine AJ, Mackintosh FC (2002) Dynamics of viscoelastic membranes. *Phys Rev E* 66(6):061606.
- Bender CM, Orszag SA (1999) *Advanced Mathematical Methods for Scientists and Engineers I* (Springer, New York).